Dynamics of Surface Crystallization and Melting in Polyethylene and Poly(ethylene oxide) Studied by Temperature-Modulated DSC and Heat Wave Spectroscopy

T. Albrecht, S. Armbruster, S. Keller, and G. Strobl*

Fakultät für Physik, Albert-Ludwigs-Universität, 79104 Freiburg, Germany

Received April 16, 2001; Revised Manuscript Received August 14, 2001

ABSTRACT: Polymers with a high longitudinal diffuse mobility within the crystallites are known to show a continuous, reversible surface melting and crystallization; temperature changes are accompanied by shifts of the crystalline−amorphous interface, resulting in a crystal thickening on cooling and a thickening of the amorphous layers on heating. In measurements of the dynamic heat capacity $c^*(\omega)$, the process shows up as a strong excess contribution which increases up to the temperature of the final irreversible crystal melting. Experiments were carried out for linear polyethylene (LPE) and poly(ethylene oxide) (PEO). Employing both a temperature-modulated differential scanning calorimeter (TMDSC) and a heat wave spectrometer (HWS), thereby covering the frequency range from 10^{-3} to 10^2 Hz, we could analyze the process dynamics. The times required for the surface melting or crystallization were deduced from the change at the signal amplitude with frequency. They are remarkably long. For temperatures near to the respective final melting points we found about 12 s for the LPE sample and 120 s for PEO. The dynamic heat capacity of PE measured by TMDSC at low frequencies corresponds to the temperature dependence of the crystallinity. A comparison with the results of a SAXS structure analysis showed perfect agreement. For PEO the quasi-stationary conditions were not reached. Even at the lowest frequencies probed by TMDSC, the dynamic heat capacity was still below the value expected on a basis of the temperature dependence of the crystallinity determined by SAXS. In determinations of the dynamic heat capacity by TMDSC and HWS, it is in general necessary to correct the raw data to account for the inner heat flow resistance, additional heat capacities, and delay times introduced by the electronics. The corrections can be accomplished by an appropriate modeling of the measuring devices.

1. Introduction

Heating of a semicrystalline polymer is in many cases accompanied by structural changes. These variations can be of different nature. First, as it is always found for metastable states, irreversible processes take place. For example, given a distribution of nonperfect crystallites of mesoscopic size with different stabilities, an irreversible melting will occur in the corresponding order at the respective melting points. On the other hand, an increase in the temperature can also initiate an improvement of order, for example by a removal of inner defects or a continuous irreversible crystal thickening. Besides these irreversible processes, one finds as a peculiar feature also reversible structure variations. They reflect the existence of local equilibria between the crystalline and fluidlike parts in semicrystalline polymers which both deviate in their properties from the ideal states represented by a macroscopic crystal and a homogeneous melt. Temperature variations lead to changes in the local equilibria and readjustments of the local structure.

Measurements of the "dynamic heat capacity" coming up during the past decade present a new tool to study these structural variations, both with regard to their extent and for analyzing the process dynamics. There are two different routes, and they provide different insights. In "quasi-isothermal" experiments one probes the reaction of a sample onto an imposed oscillating temperature

$$T^*(t) = \bar{T} + \delta T_0^* e^{i\omega t} \tag{1}$$

whereby the mean temperature $\bar{T}$ is kept constant. The programmed temperature induces an oscillating, in general phase-shifted heat flow

$$P^*(t) = \bar{P} + \delta P_0^* e^{i\omega t} \tag{2}$$

The dynamic heat capacity of the sample, C^*, expresses the ratio between the amplitudes of the heat flow and the heating rate

$$\frac{dT}{dt} = i\omega\delta T_0^* e^{i\omega t} \tag{3}$$

as

$$C^*(\omega) = \frac{\delta P_0^*}{i\omega\delta T^*_0} \tag{4}$$

The normally used dynamic heat capacity per unit mass, c^*, follows as

$$c^* = \frac{C^*}{m} \tag{5}$$

with m as sample mass. c^* is in general a complex, frequency dependent quantity, and we write

$$c^*(\omega) = c'(\omega) - ic''(\omega) = |c^*|(\omega)e^{-i\varphi_c(\omega)} \tag{6}$$

Different devices are in use and results for different polymers were reported by Wunderlich et al.,[1] Schick et al.,[2] Androsch,[3] or Saruyama,[4] selecting some typical examples out of a larger number. The works demonstrate the existence of reversible structural changes in semicrystalline polymers as a general phenomenon.

In a second type of experiment, the programmed temperature is set up of a superposition of a heating

* Corresponding author.

10.1021/ma0106595 CCC: $20.00
Published on Web 10/24/2001

with a constant rate, β, and an oscillating part

$$T^*(t) = T(t = 0) + \beta t + \delta T_0^* e^{i\omega t} \qquad (7)$$

In these experiments, both reversible and irreversible structural changes give a contribution to the signal. As was pointed out in a study of syndiotactic polypropylene by Schawe and Strobl,[5] a dominant contribution to the dynamic signal arises during the actual time of melting of a crystallite and then represents the variation with temperature of the rate of melting. In analogy to the heating run, when cooling with a constant rate, the temperature dependence of the rate of crystallization shows up in the signal. This was shown in works of Toda et al.[6]

Carrying out quasi-isothermal temperature-modulated DSC measurements in an investigation of several semicrystalline polymer systems, we have compared the amplitudes of the dynamic heat capacity in the melting ranges.[7] Particularly high signals were found for polyethylene (PE) and poly(ethylene oxide) (PEO). Both are polymers known to exhibit a reversible surface crystallization and melting.[8] This peculiar process exists under the prerequisite of a high chain mobility within the crystallites, because only then, when chains can slide through, does a rearrangement of the fold surface become possible. The increase with temperature of the entropic forces acting from the entangled amorphous regions onto the chains in the crystallites produces a melting of a certain surface layer. The process becomes reversed, i.e., turns into a crystallization, when the temperature is decreased again. Existence of this process was first suggested by Fischer,[9] then described in an improved theory by Mansfield and Rieger[10] based on experimental results provided by Tanabe et al.,[11] and was finally treated both experimentally and theoretically by Albrecht and Strobl.[12] Hu et al. therefore suggested that the particularly high values of the dynamic heat capacity observed for PE and PEO might originate from the surface crystallization and melting in these materials. The speculation was supported by an estimate based on the published structural data. A recently completed work of Goderis et al.[13] provides further support for the assignment. Authors complemented measurements of the dynamic heat capacity of PE by experiments at a synchrotron radiation source, determining in real-time the variations in the small-angle X-ray scattering and wide-angle X-ray patterns following from an oscillating temperature. The focus of the data analysis was on the phase relation between the intensity fluctuations in the scattering patterns and the temperature oscillation, and this phase relation turned out as being indicative for a surface melting.

In the work described in this paper, we continued the investigation of the surface melting and crystallization in PE and PEO in two different respects. First, we aimed for a quantitative comparison between structural data obtained by small-angle X-ray scattering and dynamic calorimetric data. Second, we tried to learn about the dynamics of surface melting and crystallization, i.e. to determine the time associated with this process. We used in our investigations two different devices for measurements of dynamic heat capacities, a temperature-modulated differential scanning calorimeter (TMDSC) and a newly constructed heat wave spectrometer (HWS). Employing both devices we covered altogether a frequency range from 10^{-3} to 10^{2} s^{-1}.

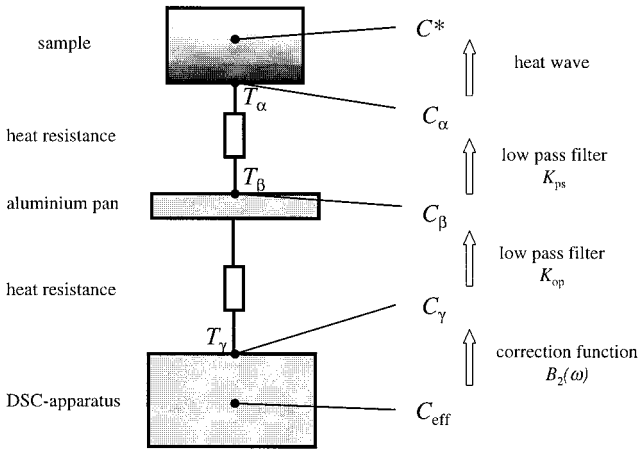

Figure 1. Model of the DSC used in the determination of the true dynamic heat capacity C^* of a sample.

As it turned out, the rates associated with surface crystallization and melting in PE and PEO happen to fall into this range.

Experimental Section

2.1. Temperature-Modulated Differential Scanning Calorimetry. Measurements of the dynamic heat capacity at very low frequencies, corresponding to periods above 1 min, were carried out with the aid of a Perkin-Elmer DSC4, using a program extension which enables oscillatory variations of the programmed temperature to be realized. We used the same program for setting the temperature and the same registration of the resulting heat flow as in the previous work,[5] the only difference being that at this time a Perkin-Elmer DSC7 was employed. As all the technical details are the same, they do not need to be repeated here.

We carried out "quasi-isothermal" measurements, i.e., performed temperature oscillations around a fixed average temperature. The mean temperature was changed stepwise, thereby passing through the whole melting range. Dynamic measurements carried out with a DSC in general yield as a result an "effective dynamic heat capacity", C_{eff}, which differs from the interesting true dynamic heat capacity c^* of the sample. Data are usually affected by properties of the measuring device. In particular, the heat flow meets various points of transfer with a nonvanishing resistance, and the electronics of the apparatus reacts with certain delay times. Only for very low frequencies, i.e., periods clearly above all inner reaction times of the apparatus, one obtains the dynamic heat capacity of the sample directly. Confining oneself to this case, however, would lead to a strong limitation of the frequency range. The problem can be solved by a procedure recently developed by Merzlyakov.[14] He succeeded to set up a model of the Perkin-Elmer DSC which includes all important parameters and is still simple enough for routine uses. On the basis of the model, the dynamic heat capacity of the sample can be extracted out of measured frequency dependent data. The model is depicted in Figure 1 with its components being described. The temperature oscillations at the different points, α, β, and γ, differ from each other and so do as a consequence the associated apparent heat capacities

$$C_i = \frac{\delta P_0^*}{i\omega\delta T_{0i}} \quad i: \alpha, \beta, \gamma \qquad (8)$$

The difference between the apparent heat capacity C_γ which would be found at the heating plate (point γ) and the effective heat capacity C_{eff} is a basis property of the apparatus. Importantly, as was pointed out by Merzlyakov, this effect of the apparatus is not dependent on the shape or mass of the aluminum pan filled with the sample but represents an intrinsic property of the calorimeter. The relation between C_γ

and C_{eff} can be expressed by use of a complex function $B_2(\omega)$, as

$$C_\gamma(\omega) = B_2(\omega) \times C_{\text{eff}}(\omega) \tag{9}$$

This basic correction function depends on the frequency ω of the applied temperature oscillations, acts on both the modulus and the phase and increases with ω. In the limit of static measurements ($\omega \rightarrow 0$) B_2 tends toward unity. We determined $B_2(\omega)$ employing the procedure suggested by Merzlyakov.[14]

In the next step of the correction, the heat flow resistancies between the heating plate and the aluminum pan (thermal conductivity K_{op}) and between the pan and the sample (thermal conductivity K_{ps}) are taken into account. The heat flow from the pan into the sample (points β and α) can be written as

$$P^*(t) = K_{\text{ps}}(T_\alpha - T_\beta) \tag{10}$$

or, for the oscillating part

$$\delta P_0^* = K_{\text{ps}}(\delta T_{0\alpha}^* - \delta T_{0\beta}^*) \tag{11}$$

A combination of eqs 8 and 11 yields

$$\delta P_0^* = K_{\text{ps}}\left(\frac{\delta P_0^*}{i\omega C_\alpha} - \frac{\delta P_0^*}{i\omega C_\beta}\right) \tag{12}$$

K_{ps} thus determines the relation between the apparent heat capacities C_β and C_α, as

$$C_\beta = \frac{C_\alpha}{1 - \frac{i\omega}{K_{\text{ps}}}C_\alpha} \tag{13}$$

In the static limit $\omega \rightarrow 0$ C_β becomes equal to C_α. The heat resistance between the heating plate and the pan (points γ and β) can be treated in analogous manner, with the only difference that the heat capacity of the aluminum pan, C_{Alu}, has to be taken into account additionally. For a thermal conductivity K_{ps}, C_γ can be expressed in terms of C_β and C_{Alu} as

$$C_\gamma = \frac{C_\beta + C_{\text{Alu}}}{1 - \frac{i\omega}{K_{\text{op}}}(C_\beta + C_{\text{Alu}})} \tag{14}$$

Equations 9, 13, and 14 used together relate the measured quantity $C_{\text{eff}}(\omega)$ with $C_\alpha(\omega)$.

Finally, one has to make sure that there are no heat waves inside the sample. For low sample masses and slow-temperature modulations, this is indeed the case. Then the true dynamic heat capacity per unit mass of the sample, c^*, can be derived from C_α by

$$c^* = \frac{C^*}{m_s} = \frac{C_\alpha}{m_s} \tag{15}$$

where m_s is the sample mass.

The conductivities K_{op} and K_{ps} are at first unknown. They can generally be derived by an adjustment of frequency dependent effective heat capacities measured for samples in the molten state. In the melt, the specific heat capacity c^* is known to be real valued and independent of ω. For $C_\gamma(\omega)$, as it follows after applying the basic apparatus correction eq 9, the frequency dependence of the data arises only from the two parameters K_{op} and K_{ps}. Figure 2 gives an example how the heat conductivities were determined. The quantity C_γ is given in the figure by its modulus and phase. The curves passing through the experimental points were calculated on the basis of the given equations, employing a standard nonlinear fitting

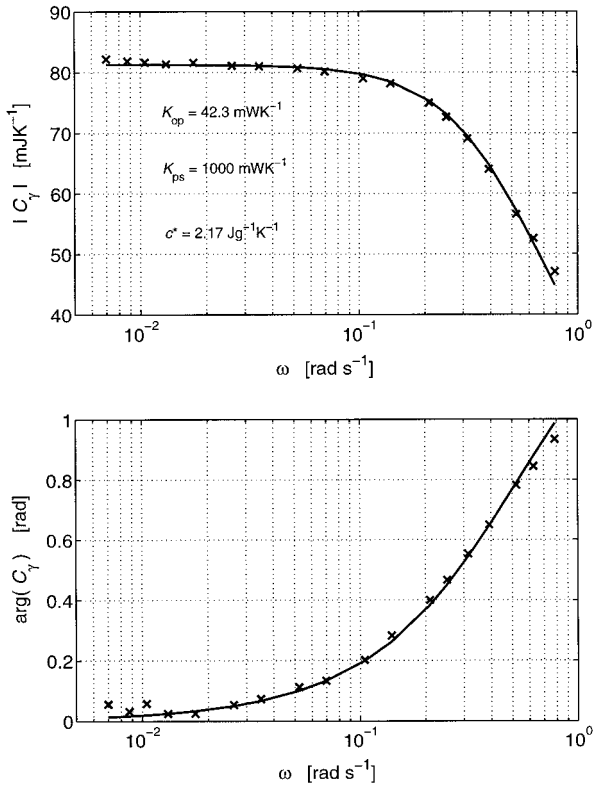

Figure 2. Sample of PEO in the melt (74 °C): Frequency dependence of the modulus and the phase of the apparent heat capacity C_γ. Values of the parameters K_{op}, K_{ps}, and c^* were derived from the fits.

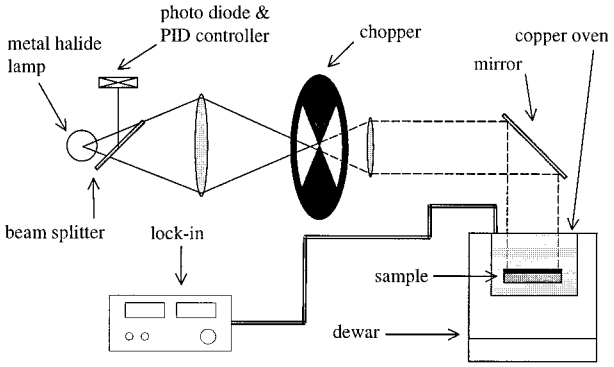

Figure 3. Experimental setup of the light-driven heat wave spectrometer. The light intensity of a lamp is modulated by a chopper. An absorber transforms it into a heat wave which propagates through the sample. The amplitude and phase of the heat wave are measured at the top directly below the absorbance layer, yielding the effusivity, and at the bottom, which gives the diffusivity.

algorithm. From the fits we derived the indicated values K_{op} and K_{ps}. As demonstrated by the results, effects of the finite times necessary for the heat transfers between the different parts of the apparatus are at first observed in the phase, and then for frequencies ω above 10^{-1} s^{-1} also in the modulus of C_γ. A period on the order of 10 s obviously represents a lower limit for temperature modulations in this DSC. For shorter periods, corrections get too strong and the accuracy of the extracted sample heat capacity is too low.

2.2. Heat Wave Spectrometer. For measurements of the dynamic heat capacity at higher frequencies we constructed a "heat wave spectrometer". As it has already been described in detail in a recent paper,[15] we confine ourselves here to a brief sketch of the main features. The setup of the device is depicted in Figure 3. Using a metal halide lamp as a light source, platelike samples with an absorbance layer (graphite or a

sputtered CrN film) at the surface become heated, whereby power modulations are produced by a chopper with rates of rotation in the range from 0.01 Hz to 1 kHz. The periodic heat flux initiates thermal waves which penetrate into the sample. The resulting temperature oscillations are measured both at the surface, in direct contact with the absorbance layer, and at the bottom. We use either a tiny (12 μm) thermocouple or a gold film sputtered on a glass slide which acts as a temperature-dependent resistor. To allow for variations of the mean temperature the sample is placed in an oven. The voltage oscillations are registered by amplitude and phase with a lock-in amplifier, which obtains the reference signal from the chopper. While working with the meander-like power modulation produced by the chopper, using the lock-in amplifier at the rotation frequency of the chopper implies to just measure the response to the basic Fourier component. Possibly existing nonlinear parts in the response are also not registered.

The relevant equations dealing with this situation can be summarized as follows. The oscillating heating power applied to the surface

$$P^*(t) = \bar{P} + \delta P_0^* \exp(i\omega t) \tag{16}$$

produces a planar temperature wave in the sample given by

$$\delta T^*(z, t) = \delta T_0^* \exp(\mathrm{i}(\omega t - k^* z)) \tag{17}$$

z is the propagation direction, and k^* is a complex wave vector. Solving the temperature diffusion equation leads to

$$k^*(\omega) = \sqrt{\frac{-\mathrm{i}\omega}{D}} = \sqrt{\frac{\omega}{D}} \exp\left(-i\frac{\pi}{4}\right) \tag{18}$$

where D denotes the diffusivity.

Accounting for the boundary condition that all the produced heat has to flow into the sample, one is led to the following relation between the amplitude of the heat flux oscillation $\delta P_0^*/S$ (S is the illuminated area) and the amplitude δT_0^* of the temperature oscillation at the surface:

$$\delta T_0^* = \frac{\delta P_0^*}{S} = \frac{\exp\left(-i\frac{\pi}{4}\right)}{\sqrt{\omega}\sqrt{\epsilon}} \tag{19}$$

Here ϵ denotes the effusivity. If the temperature oscillation is measured at the bottom of a sample with thickness d, it is given by

$$\delta T^*(z = d, t) = \frac{\delta P_0^*}{S} \frac{\exp\left(-i\frac{\pi}{4}\right)}{\sqrt{\omega}\sqrt{\epsilon}} \exp\, i\left(\omega t - \sqrt{\frac{\omega}{2D}}\, d\right) \exp\left(-\sqrt{\frac{\omega}{2D}}\, d\right) \tag{20}$$

According to eqs 19 and 20, one can derive the effusivity from the amplitude of the temperature oscillation at the surface and the diffusivity from a phase measurement at the bottom of the sample.

Effusivity and diffusivity are generally related to the specific heat c and the thermal conductivity κ, by

$$\epsilon = \rho\kappa c \tag{21}$$

and

$$D = \frac{\kappa}{\rho c} \tag{22}$$

So far we dealt with a real valued dynamic heat capacity only. For a complex dynamic heat capacity, the effusivity and the diffusivity become frequency dependent and complex as well. Equations 21 and 22 remain valid. Therefore, from a measurement of both $\epsilon^*(\omega)$ and $D^*(\omega)$, one can always deduce the heat capacity and thermal conductivity, as

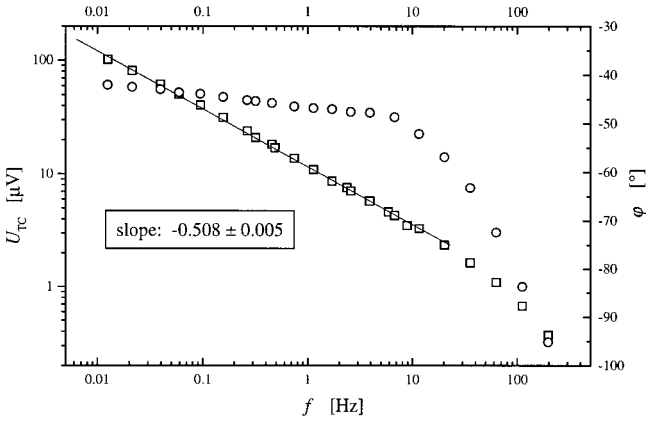

Figure 4. Frequency dependence of the temperature signal measured by a thermocouple at the top of the sample. Amplitude U_{TC} (squares) and phase shift φ (circles) with regard to the light intensity.

$$c^*(\omega) = \frac{1}{\rho}\sqrt{\frac{\epsilon^*(\omega)}{D^*(\omega)}} \tag{23}$$

$$\kappa^*(\omega) = \sqrt{\epsilon^*(\omega) D^*(\omega)} \tag{24}$$

Employing the heat wave spectrometer, we proceed along this way.

Figure 4 gives an example for the performance of the device. A glass slide was covered with a graphite layer and the temperature oscillation in the layer was registered with an attached thermocouple. According to eq 19 one expects a phase shift relative to the applied heating power of $-45°$ and an amplitude which is inversely proportional to the square root of the chopper frequency. This is confirmed by the observations, for the amplitude nearly over the full range and for the phase up to 10 Hz. The deviations in the range of higher frequencies are due to the heat capacity of the thermocouple and the heat flow resistance of the point of attachment. The gold-film sensor gives a better performance and shows no deviations from ideal behavior up to 100 Hz.

2.3. Small-angle X-ray Scattering. SAXS experiments were conducted at a conventional X-ray source with the aid of a Kratky camera, which was equipped with a temperature-controlled sample holder. The changes of the structure during heating were followed measuring the scattering curves with a position-sensitive metal wire detector. Deconvolution of the slit-smeared data was achieved applying an algorithm developed in our group.[16]

Partially crystalline polymers like PE and PEO are set up of stacks of thin laterally extended crystallites. Here, the scattering intensity can be related to the one-dimensional electron density (ρ_e) correlation function $K(z)$ defined as

$$K(z) = \langle(\rho_e(z) - \langle\rho_e\rangle)(\rho_e(0) - \langle\rho_e\rangle)\rangle = \langle\rho_e(z)\rho_e(0)\rangle - \langle\rho_e\rangle^2 \tag{25}$$

It can be directly obtained by a Fourier transformation of the scattering intensity. If we use the scattering cross-section per unit volume $\Sigma(q)$, $K(z)$ follows as

$$K(z) = \frac{1}{r_e^2}\frac{1}{(2\pi)^3}\int_0^\infty \cos\, qz \cdot 4\pi q^2 \Sigma(q)\mathrm{d}q \tag{26}$$

q denotes the scattering vector, being related to the Bragg-scattering angle ϑ_B by

$$q = \frac{4\pi}{\lambda}\sin\vartheta_B \tag{27}$$

(r_e: classical electron radius).[17]

A trajectory along the surface normal passes through amorphous regions with an electron density $\rho_{e,a}$ and crystallites with a core density $\rho_{e,c}$. As shown by Ruland,[18] for such a layer system the second derivative of the correlation function, $K''(z)$, gives the distribution of distances between interfaces, in the form

$$K''(z) = \frac{O_{ac}}{2}\Delta\rho_e^{\,2}\,[h_a(z) + h_c(z) - 2h_{ac}(z) + h_{aca}(z) + h_{cac}(z)\cdots] \quad (28)$$

The expression between the brackets is set up of a series of distribution functions, whereby the subscripts indicate which phases, amorphous and crystalline ones, are to be traversed while going from one interface to the other. Of main importance are the first three contributions. They give the distributions of the thickness of the amorphous and the crystalline layers respectively (h_a, h_c) and of the sum of both (h_{ac}) which is identical with the long spacing L. Rather than by calculating the second derivative of the correlation function, $K''(z)$ can also be deduced directly from the measuring data, by use of

$$K''(z) = \frac{2}{r_e^{\,2}(2\pi)^2}\int_0^\infty [\lim_{q\to\infty} q^4\Sigma(q) - q^4\Sigma(q)]\cos qz\,dq \quad (29)$$

SAXS experiments also enable the crystallinity to be determined. One generally obtains the "linear crystallinity" , as

$$\phi_l = \frac{d_c}{L} \quad (30)$$

with d_c as crystal thickness and L as long spacing. ϕ_l describes the volume fraction occupied by the crystalline lamellae within one stack.

2.4. Samples. The PE sample under study was a high molar mass linear polyethylene (density 0.96 g cm^{-3}, melt flow index: 0.2; trade name Lupolen 6011) produced by BASF AG (Ludwigshafen, Germany).

In the case of PEO, we investigated two different materials, both having the same weight-average molar mass $M_w = 3 \times 10^5$ g mol^{-1}. They were purchased from Aldrich Chemicals Co and Polymer Standard Service. The Aldrich sample included anorganic additives. They had no effects on the thermal properties but rendered the X-ray scattering experiments more difficult, due to a superposition of a strong second scattering component. The difficulties did not arise for the second sample, which was free of additives.

Results

We measured the dynamic heat capacity for PE and PEO in quasi-isothermal experiments. The mean temperature, being changed step for step, was varied throughout the whole melting range of the samples. We used TMDSC for low frequencies corresponding to periods between 60 and 1000 s and HWS for the range of higher frequencies, from 10^{-2} to 1 Hz.

SAXS structure determinations were carried out for samples with similar thermal treatments. The experiments yielded the crystal thickness and the long spacing as a function of temperature. We determined in this way the amount of surface melting during heating and surface crystallization during cooling and compared it with the dynamic calorimetric data.

3.1. Dynamic Heat Capacity of PE. 3.1.1. Measurement by TMDSC. The PE sample was isothermally crystallized at 124 °C. After completion, the sample was heated to 130 °C, which is 5 deg below the DSC melting peak, and was kept there for 1 day. The latter procedure is necessary to stabilize the structure. Working with PE, one has always to be aware of the ongoing solid state thickening of the lamellae. As it follows a logarithmic time dependence, the thickening comes practically to an end after a 1 day annealing. The morphology of thus treated samples remains constant during cooling and reheating, as long as one does not surpass the annealing temperature. The only structure changes which then occur during cooling and reheating are surface melting and crystallization.

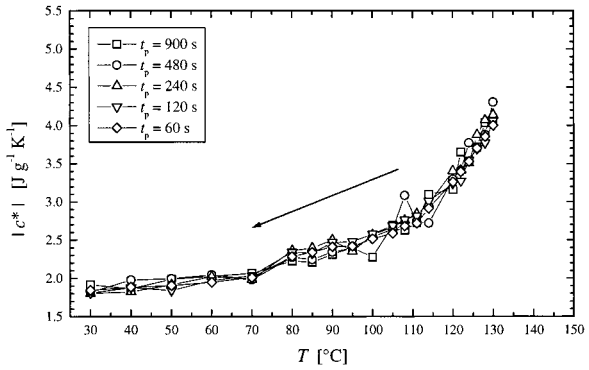

Figure 5. PE, isothermally crystallized at 124 °C and annealed at 130 °C: Modulus of the dynamic heat capacity extracted from the TMDSC signal as obtained during a stepwise cooling (modulation amplitude: 0.5 °C, periods as indicated).

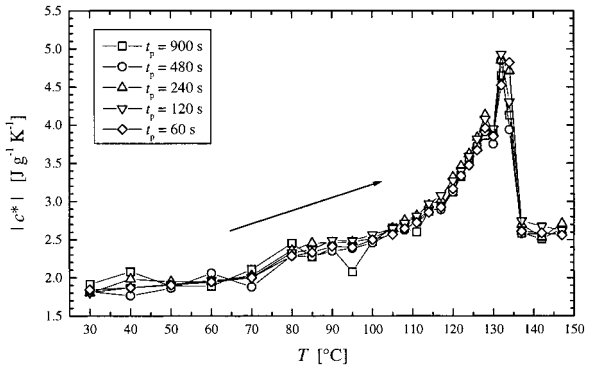

Figure 6. Same experiment as Figure 5. Results obtained during a subsequent heating to the melt.

Figure 5 shows dynamic heat capacities measured during the cooling process for different modulation periods between 60 and 900 s. These are the final results, extracted from the measured data by application of the correction algorithm which accounts for all the inner heat transfers and electronic time delays. The amplitude of the temperature modulation was always $\delta T = 0.5$ °C. The detected amplitude of the dynamic heat capacity $|c^*|$ begins with a rather high value at the starting temperature 130 °C and then decreases continuously down to a value below 2 J g^{-1} K^{-1}. The value does not change with the modulation period; i.e., it is frequency independent.

Figure 6 depicts the modulus of the dynamic heat capacity during a subsequent stepwise heating. One observes the same values as during the cooling, up to the annealing temperature of 130 °C. If the heating then is continued one observes, after passing through a minimum, a further strong increase. Finally, the dynamic heat capacity drops down to a constant value of 2.5 J g^{-1} K^{-1}. As a comparison with literature data shows,[19] we find here the specific heat of the melt. Here, in the equilibrium state, the dynamic heat capacity originates from rapid vibrational and relaxatory motions only and then agrees with the value found in standard DSC runs with a constant heating rate.

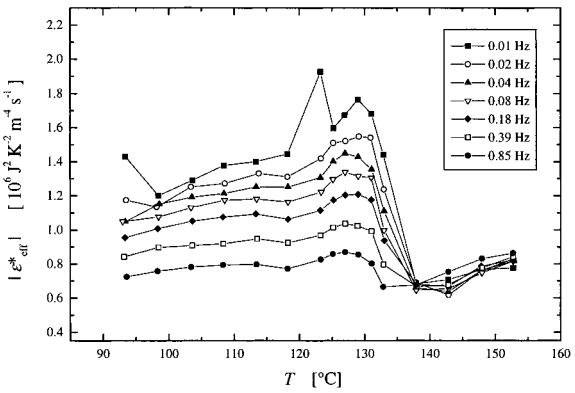

Figure 7. PE, isothermally crystallized at 120 °C and cooled to 90 °C: Effective effusivity, determined by HWS at various frequencies during a stepwise heating.

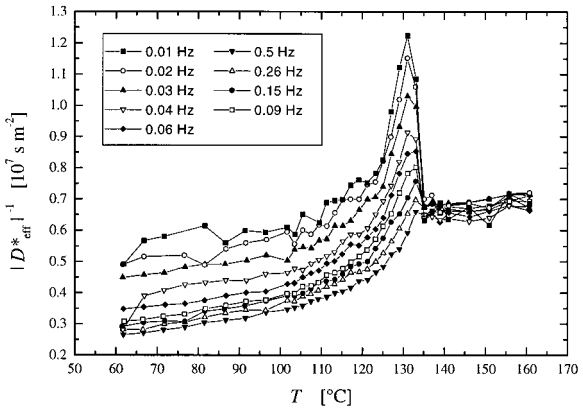

Figure 8. PE, isothermally crystallized at 120 °C and cooled to 60 °C: Effective reciprocal diffusivity, determined by HWS at various frequencies during a stepwise heating.

3.1.2. Determination by HWS. Measurements of the effusivity and the diffusivity in the heat wave spectrometer cannot be carried out with one sample only. For effusivity determinations, the sample has to be thick enough so that the measurement is not perturbed by the superposition of heat waves reflected at the bottom. This is certainly fulfilled when the thickness is larger than several wavelengths. For the chosen thickness, 8 mm, this was ensured for the lowest used frequency. The diffusivity measurement meets an opposite requirement. A signal with a sufficiently high amplitude at the bottom of the sample can only be measured if the number of wavelengths over the sample thickness is small. To have this condition fulfilled, it may even be necessary to choose samples of different thicknesses for the high and the low ends of the frequency range of the spectrometer. In our case, good results throughout were obtained for a thickness of 30μm. Measurements were carried out for a sample isothermally crystallized at 120 °C, which after completion was cooled to the lower starting temperature. The absorption of the light generally leeds to a temperature increase of the sample surface with regard to the preset temperature of the sample holder. For the chosen light intensities, the gradient between the surface and the bottom amounted for the thick samples of the effusivity measurements to some degrees. The gradient could be determined, and the temperatures given in the following are always those referring to the absorption layer at the top of the sample. The lowest frequency in the HWS measurements was 10^{-1} Hz and overlapped with the highest frequencies achieved by the TMDSC. Figure 7 depicts the effusivities derived from the amplitude of the temperature fluctuations at the top of the sample by application of eq 19. Measurements were carried out during a stepwise heating beginning at 93 °C. Figure 8 shows the results of a corresponding measurement of the diffusivity. The reciprocal value of the modulus of the diffusivity was derived from the phase difference between the temperature oscillation at the bottom of the sample and the oscillation of the light power at the surface, based on eq 20. Interesting to note, both quantities, the effusivity and the (reciprocal) diffusivity, show a pronounced frequency dependence for all temperatures below the final melting in the frequency range probed by the spectrometer. As expected, the frequency dependence disappears in the melt.

Surprising at first, we observe also a frequency dependence at low temperatures, away from the main melting range, and indeed further cooling did not remove it. As it turned out, this behavior depended on the preparation, and does not represent a property of the sample. It is due to an imperfect contact between the thermocouple and the sample after the crystallization. The thermocouple was fixed in a molten state, also with the aid of a drop of a glue, but the contact always somewhat deteriorated on cooling, as a consequence of the sample shrinkage. The effect of the nonvanishing heat flow resistance between the thermocouple and the sample surface is not the same on the top and on the bottom. On the top, the thermocouple becomes heated in direct contact with the absorbance layer, but then a temperature difference can arise between the thermocouple and the sample surface, due to the nonvanishing heat transfer resistance. As a consequence the measured amplitude of the temperature oscillation is higher than that on the sample surface. On the bottom we find an opposite tendency. Again we have some heat transfer resistance between the sample surface and the thermocouple, but now it leeds to a lowering of the signal amplitude and, more important for the evaluation, an additional delay in the phase of the signal. We dealt with this situation by introducing two empirical frequency (f) dependent "transfer functions" . They were used to correct the measured effective temperature amplitude $\delta T^*_{0,\mathrm{eff}}$ and the effective phase delay φ_{eff} to obtain the corresponding quantities at the sample surfaces, δT^*_0 and ϕ. The correction function for the effusivity measurements, $a(f)$, is given by

$$a(f) = \frac{|\delta T^*_{0,\mathrm{eff}}|(f)}{|\delta T^*_0|(f)} \tag{31}$$

and that for the diffusivity measurement by

$$\Delta\varphi(f) = \varphi_{\mathrm{eff}}(f) - \varphi(f) \tag{32}$$

We determined the two functions at the lowest achieved temperature assuming that at this temperature there should be no reversible melting and crystallization and therefore also no frequency dependence in the effusivity and diffusivity. Figures 9 and 10 depict the thus obtained correction functions. There remains, however, a second problem. During heating, the crystallinity changes, and finally, in the melt, as shown by the lack of any frequency dependence, the contacts are again ideal. This implies that the correction functions are not constant but change during heating. As there is no way

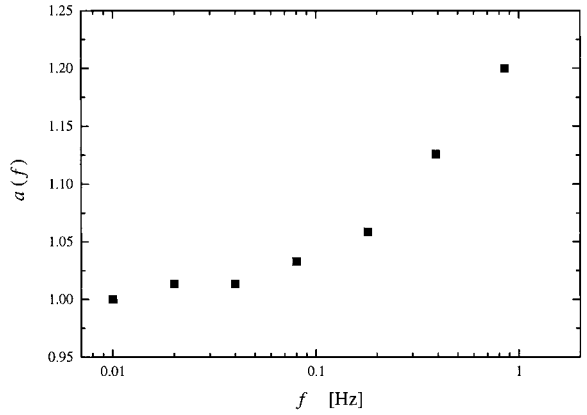

Figure 9. Correction factor $a(f)$ applied to account for the heat transfer resistance between the upper surface of the crystallized sample and the thermocouple.

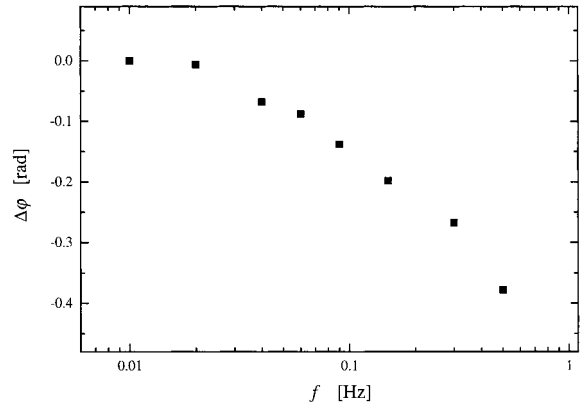

Figure 10. Correction $\Delta\varphi$ of the phase of the signal measured at the bottom of the crystallized sample. The correction has to be introduced to account for the heat transfer resistance between the surface and the thermocouple.

to determine this change we used the simplest possible equation showing the correct limiting behavior and set for the temperature dependence of the correction factor a

$$a(f, T) = a(f, T_0)\frac{\phi(T)}{\phi(T_0)} \tag{33}$$

and for the temperature dependence of the correction function $\Delta\varphi$

$$\Delta\varphi(f, T_0) = \Delta\varphi(f, T_0)\frac{\phi(T)}{\phi(T_0)} \tag{34}$$

We applied these correction functions to the first measured "effective" effusivities and diffusivities and obtained the corrected values shown in Figures 11 and 12. Important to note, also after the correction we clearly see a pronounced frequency dependence in both quantities arising in the regions of the melting peak. The correction just removed the artifact in the effective data of a frequency dependence persisting down to low temperatures. It is clear that different from the TMDSC measurements which probe lower frequencies we can now, using the HWS, indeed observe the dynamics of the process.

The next step, also necessary for a comparison of the HWS− with the TMDSC data, is the derivation of the dynamic heat capacity. This is possible by applying eq

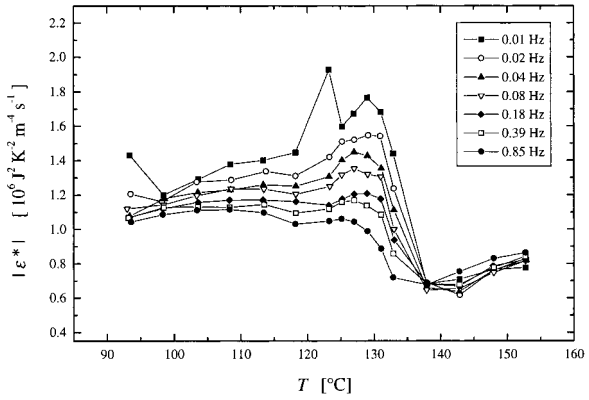

Figure 11. Measurement of Figure 7: True effusivity obtained after a correction of the temperature amplitude by the factor $a(f)$.

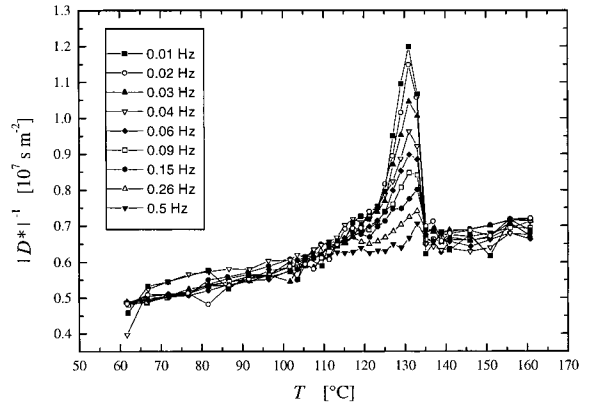

Figure 12. Measurement of Figure 8: True reciprocal diffusivity obtained after a correction of the phase by $\Delta\varphi$.

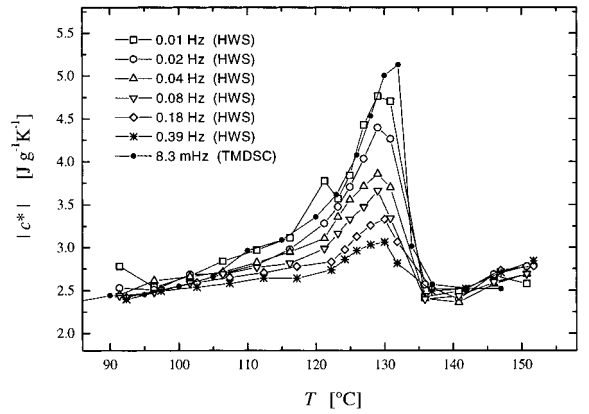

Figure 13. PE: Frequency dependent modulus of the dynamic heat capacity, derived from the data in Figures 11 and 12.

23. Furthermore, using eq 24, one can also determine the thermal conductivity κ. The results are presented in Figures 13 and 14. For the heat conductivity, we obtain just a step located at the melting peak. Obviously the heat conductivity does not show a frequency dependence; the variations are within the error limits of the measurement. On the other hand, we find a pronounced frequency dependence in the modulus of the dynamic heat capacity. For the highest frequencies used, the signal is near to a complete disappearance. The figure includes also the results of a TMDSC measurement at 8.3 mHz which is adjacent to the lowest frequency measured by HWS (0.01 Hz). The results of the two measurements perfectly follow each other; the TMDSC

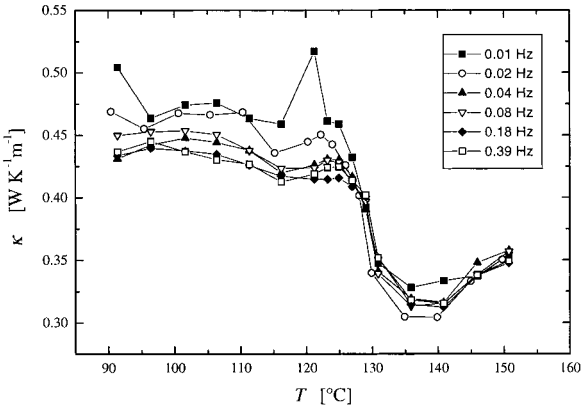

Figure 14. PE: Heat conductivity derived from the data in Figures 11 and 12.

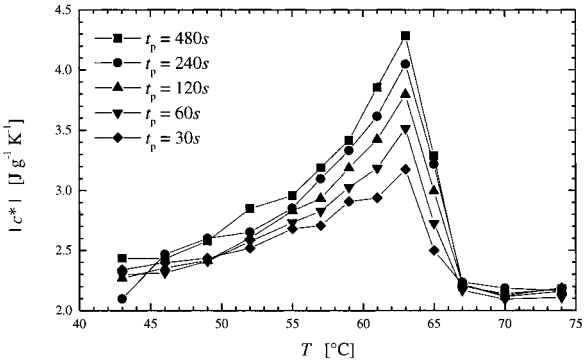

Figure 15. PEO, isothermally crystallized at 48 °C and cooled: Modulus of the dynamic heat capacity extracted from the TMDSC signal as obtained during a stepwise heating (modulation amplitude, 0.5 °C; periods as indicated).

value obtained for a slightly lower frequency is just somewhat higher than the HWS result. The comparison gives us confidence that the empirical procedure applied to correct the imperfect contact between thermocouple and sample surface is essentially alright.

3.2. Dynamic Heat Capacity of Poly(ethylene oxide). 3.2.1. Measurement by TMDSC. A PEO sample was isothermally crystallized at 48 °C and cooled. Figure 15 shows the result of measurements of the dynamic heat capacity during a successive stepwise heating. The modulation period was varied between 30 and 480 s. As we see, one finds for PEO again a strong signal with a maximum in the melting range, but now, contrasting the observations for PE, we have also in the frequency range of the TMDSC a frequency dependence.

3.2.2. Determination by HWS. HWS measurements for PEO were also carried out for a sample isothermally crystallized at 48 °C, which was then cooled to room temperature and investigated during a successive stepwise heating. Figure 16 depicts the effusivities obtained during the scan for the indicated frequencies. Effusivities increase with temperature and decrease with the frequency, until the melt is reached where a constant, low value is found. Different from PE, we now have also at low temperatures an essentially frequency independent effusivity, as it is expected. Obviously for PEO the contact between the thermocouple and the sample surfaces is not much affected by the crystallization process. This can be due to the low amount of shrinkage on crystallization and also to a better adhesion of the thermocouple on the polar PEO surface. The result of the diffusivity measurement for a sample with the same

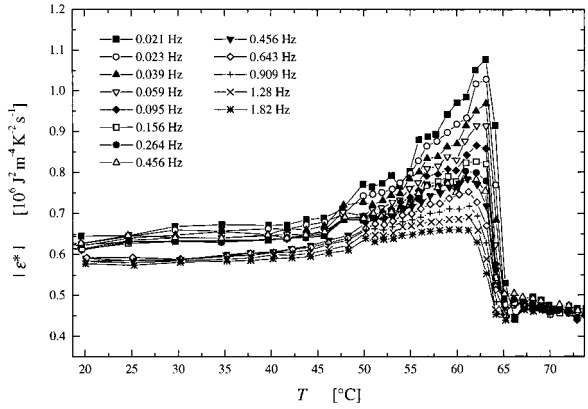

Figure 16. PEO, isothermally crystallized at 48 °C and cooled: effusivity, determined by HWS at various frequencies during a stepwise heating.

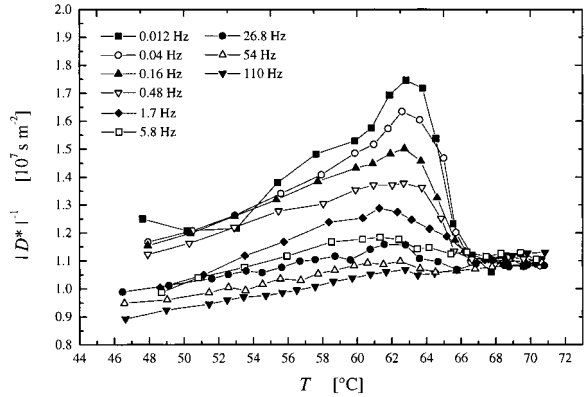

Figure 17. PEO, isothermally crystallized at 48 °C and cooled: reciprocal diffusivity, determined by HWS at various frequencies during a stepwise heating.

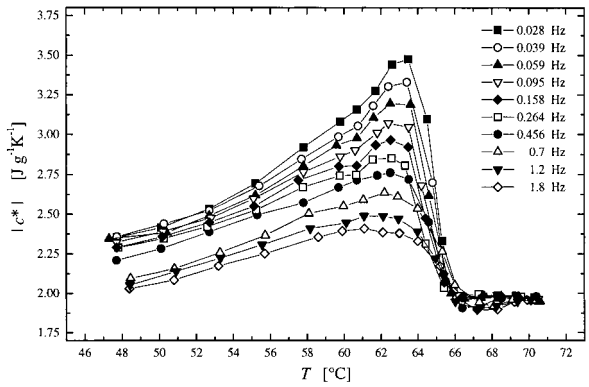

Figure 18. PEO: Frequency dependent modulus of the dynamic heat capacity, derived from the data in Figures 16 and 17.

thermal history is shown in Figure 17. As for the effusivity, we find a strong signal in the melting range, which has a pronounced frequency dependence.

The values of the dynamic heat capacity and the conductivity derived from the effusivities and the diffusivities at the various frequencies and temperatures are presented in Figures 18 and 19. As in the case of PE we find a decrease of the heat conductivity at the melting point which is frequency independent in the error limits of the measurement, and on the other side a frequency dependent dynamic heat capacity with a maximum in the range of the final melting temperature.

3.3. SAXS Investigation of Surface Melting in PE and PEO. The SAXS experiments were carried out on

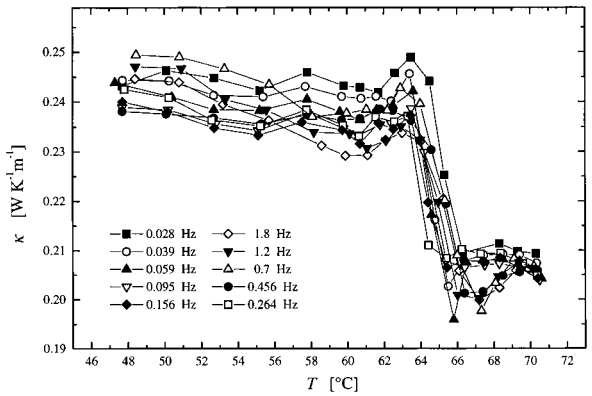

Figure 19. PEO: Heat conductivity derived from the data in Figures 16 and 17.

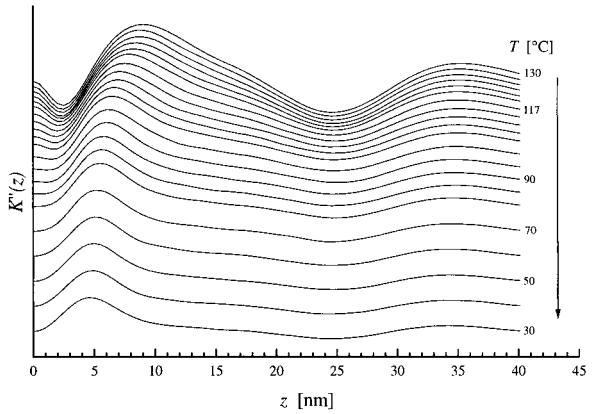

Figure 20. PE, crystallized at 124 °C and annealed at 130 °C: Interface distance distribution functions $K''(z)$ derived from SAXS curves measured during cooling.

samples of PE and PEO prepared in the same way as in the dynamic calorimetric investigations. The aim of the measurements was a quantitative characterization of the surface melting and crystallization processes going on during heating and cooling. Figure 20 presents a particularly clear result obtained for PE after a crystallization at 124 °C and a 1 day annealing at 130 °C. The figure shows the interface distance distribution functions $K''(z)$ as derived from the scattering curves measured during a cooling in immediate succession to the annealing. Curves show a peak in the range between 5 and 10 nm and a minimum located around 25 nm. The peak is to be assigned to the amorphous layers and indicates their thickness; the minimum gives the long spacing. As to be recognized, a decrease in the temperature leaves the long spacing unchanged but results in a continuous shift in the location of the amorphous layer peak to smaller values. This is exactly the behavior expected for a continuous surface crystallization. The result indicates that the interface between the crystallites and the amorphous regions becomes continuously shifted into the amorphous range. The amount of shifting is remarkably large. The amorphous layer thickness begins at the high temperatures at 9 nm and ends up at room temperature at 5 nm. Figure 21 shows this temperature dependence in detail and includes in addition the results of a measurement during a subsequent heating process. As we see, the process is practically reversible. There is some displacement to lower values, which took place during a 1 month storage at room temperature, but it is small; the form of the two curves is identical.

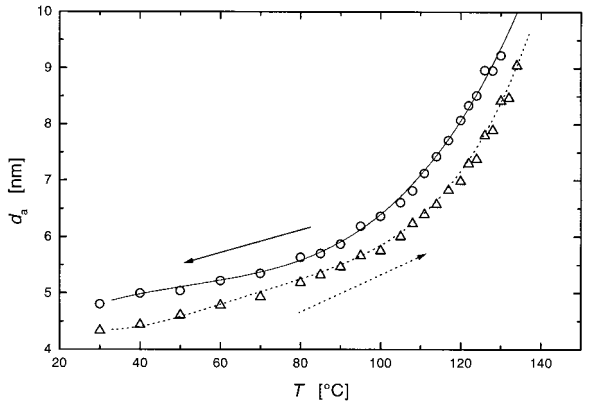

Figure 21. PE: temperature dependence of the thickness of the amorphous layers as derived from the $K''(z)$ curves shown in Figure 20 (squares). Change of d_a with temperature during a subsequent heating after a longer storage at room temperature (triangles). The two lines are guidelines for the eye.

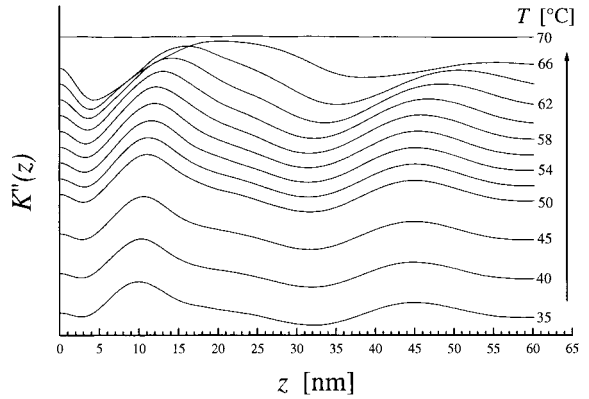

Figure 22. PEO, crystallized at 48 °C and cooled: Interface distance distribution functions $K''(z)$ derived from SAXS curves measured during heating.

SAXS experiments on PEO are more cumbersome. The electron density difference between the crystallites and the amorphous regions is three times smaller than in PE, and this means a reduction in the scattering intensity by 1 order of magnitude. For this reason the interface distance distribution functions $K''(z)$, obtained by the Fourier transformation eq 29, have in general a lower accuracy. Figure 22 gives a more favorable example. The curves wered derived from SAXS measurements carried out for a sample isothermally crystallized at 48 °C and then cooled. Again the peak reflects the amorphous layer thickness and the minimum gives the long spacing. Over a larger temperature range the long spacing remains constant, while the peak becomes shifted. Figure 23 collects the thicknesses d_a of the amorphous layers and the long spacings L derived from the interface distribution functions. For temperatures below 60 °C the change of d_a is obviously larger than the change in the long spacing which speaks in favor of a dominant role of surface melting.

Discussion

Looking at the results, we can state at first that for PE and PEO the dynamic heat capacity includes, in addition to the normal contributions originating from vibrations and rapid local relaxation processes, a second part which becomes large at temperatures near to the melting point. The finding confirms our first less accurate observations,[7] and we can now reexamine on a

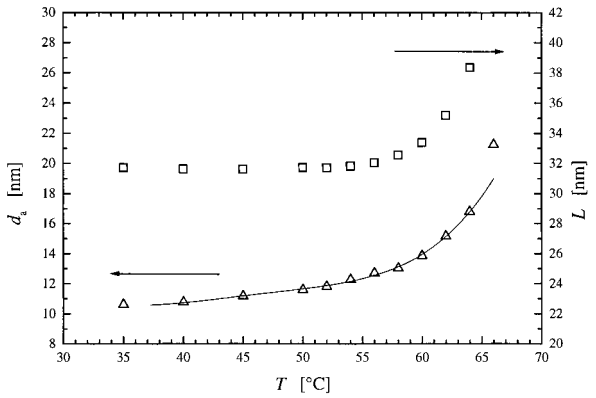

Figure 23. PEO: temperature dependence of the thickness of the amorphous layers d_a and the long spacing L as derived from the $K''(z)$ curves shown in Figure 22. The curve is a guideline for the eye.

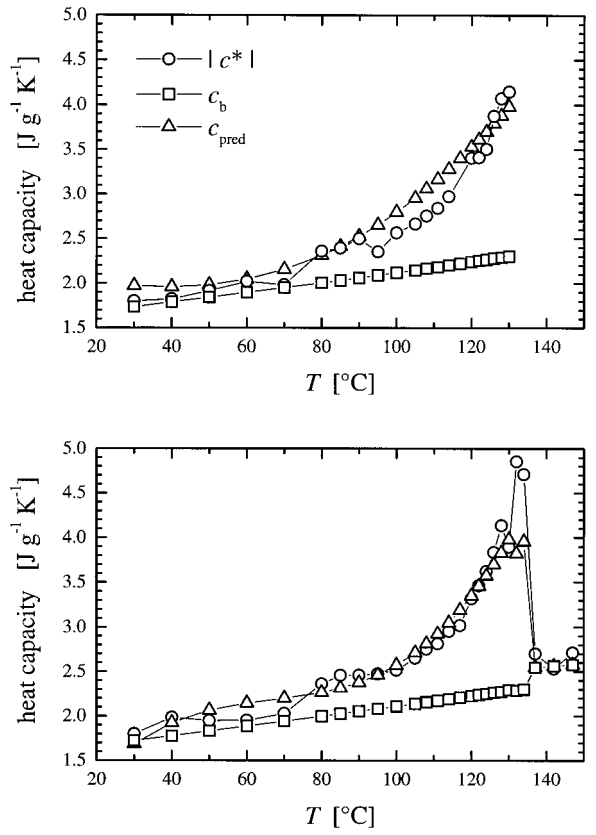

Figure 24. PE, crystallized at 124 °C and annealed at 130 °C, investigated during cooling (top) and a subsequent heating (bottom): dynamic heat capacity measured by TMDSC (t_p = 240 s). Vibrational part c_b and total dynamic heat capacity c_{pred} predicted on the basis of the temperature variation of the crystallinity as determined by SAXS.

broader experimental basis the suggestion that this "excess contribution" could originate from surface crystallization and melting. Furthermore, the experiments provide insight into the dynamics of the process.

The examination can be carried out in strict manner by a comparison with the results of the SAXS experiments. All the required data are available. Carrying out the comparison for PE leads to the result presented in Figure 24. We deal here with a sample isothermally crystallized at 124 °C and then annealed at 130 °C. The upper part refers to the cooling and the lower part to the heating process. In the comparison we use the TMDSC results only. They showed no frequency dependence and therefore represent the maximum amplitude to be measured for the dynamic heat capacity. We picked out one series of data from Figures 5 and 6, that obtained for a modulation period of 240 s. These data points are given by the circles. On the other hand, the SAXS experiments carried out for a sample with the same thermal history yielded the temperature dependence of the thickness of the amorphous layers (Figure 21) and therefore, introducing the constant long spacing (L = 25 nm), the temperature dependence of the crystallinity, just by using eq 30. As was stressed previously, the observed structural changes are indicative for a surface crystallization and melting process. In a first step, we can calculate the basic part c_b of the dynamic heat capacity, originating from the vibrations and rapid relaxations. It can be described by

$$c_b = \phi c_{cr} + (1 - \phi)c_{am} \tag{35}$$

and changes with the crystallinity. Values for the specific heats of the crystallites c_{cr} and the amorphous regions c_{am} are given in Wunderlich's ATHAS databank.[19] In the experimental temperature range c_{cr} and c_{am} can be represented by

$$c_{cr} = -0.0813 \text{ J g}^{-1} + 0.0056 \text{ J g}^{-1}\text{K}^{-1}T,\ c_{am} = 1.2800 \text{ J g}^{-1} + 0.0031 \text{ J g}^{-1}\text{K}^{-1}\ T \tag{36}$$

This basic part is indicated in the figures with square symbols. We find a smooth curve, which obviously does not reproduce the measured dynamic heat capacities. The data points indicated by triangles give the dynamic heat capacity c_{pred} predicted on the basis of the changing crystallinity. They include in addition to the basic part the excess contribution originating from the surface melting, to be described as

$$c_{exc} = -h_m \frac{d\phi}{dT} \tag{37}$$

Here, the parameter h_m denotes the heat of melting per gram, and we chose for it the value

$$h_m = 294 \text{ J g}^{-1} \tag{38}$$

c_{pred} nicely agrees for all temperatures with the measured dynamic heat capacities, both in the cooling and the heating process. Hence, we have the proof that the excess part in the dynamic heat capacity measured for PE is indeed caused by a reversible surface crystallization and melting. A deviation is observed for temperatures above the annealing temperature. Whether or not it is due to the same process or to another one cannot be told since we encounter under this situation rapid irreversible structural changes.

As demonstrated by the frequency invariance of the signal as measured in the TMDSC, the time required by the system to establish the local equilibrium at the surface of the PE crystals is shorter than the times probed by this method. Fortunately HWS, having access to shorter times, enters the characteristic time region of surface melting in PE. The results shown in Figure 13 demonstrate that the surface melting and crystallization takes place with rates which are above 10^{-1} Hz and, probably, below 1 Hz. For frequencies around 0.08 Hz the signal amplitude is reduced to half its original value which means that 12 s is the characteristic time scale associated with surface melting for the investi-

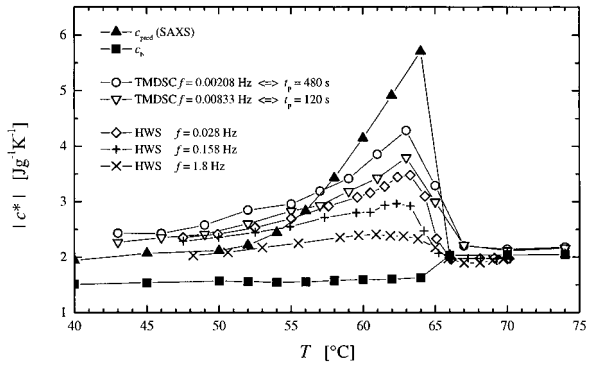

Figure 25. PEO, crystallized at 48 °C and cooled: Modulus of the dynamic heat capacity measured by TMDSC and HWS at the indicated frequencies during a stepwise heating (selection of curves from Figures 15 and 18). Dynamic heat capacity c_{pred} expected from the temperature variation of the crystallinity as determined by SAXS.

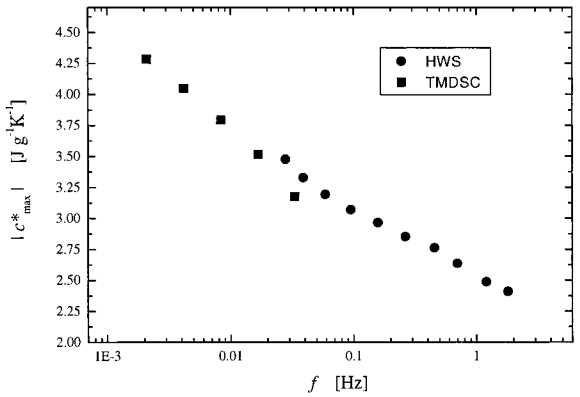

Figure 26. PEO, crystallized at 48 °C. Frequency dependencies of the peak values of the dynamic heat capacity determined by TMDSC and HWS.

gated PE sample. This time will depend on the temperature and refers as given here to 130 °C.

We can carry out the same comparison for PEO. As was already emphasized considering the results of Figure 15, here the frequency dependence of the signal is not restricted to the range of the HWS but goes on to the large modulation periods of the TMDSC. This means that the relaxation times for the reversible structural changes in PEO are much longer than those found for PE. Figure 25 collects data for the dynamic heat capacity measured by both TMDSC and HWS and includes in addition, deduced in the same way as for PE, the values c_{pred} predicted on the basis of the SAXS analysis of the structural changes with temperature. The specific heats of the crystallites and amorphous regions as well as the heat of fusion required for the calculation of the basic contribution c_b were again obtained from Wunderlich's databank[19] and chosen as

$$c_{cr} = 0.1224 \text{ J g}^{-1} + 0.0038 \text{ J g}^{-1}\text{K}^{-1}\, T,$$
$$c_{am} = 1.4534 \text{ J g}^{-1} + 0.0017 \text{ J g}^{-1}\text{K}^{-1}\, T \quad (39)$$

and

$$h_m = 197 \text{ J g}^{-1} \quad (40)$$

All data points refer to a sample which was isothermally crystallized at 48 °C. The calorimetric data were selected from the curves given in Figures 15 and 18. As already noted, the calorimetric data obtained by the two methods follow systematically one after the other. For temperatures around the melting peak c_{pred} is found lying above all measured signals, which comes as expected considering the ongoing frequency dependence. It implies that even at the highest modulation periods of the TMDSC the local equilibrium at the surfaces of the PEO crystals is not yet reached. A characteristic time can again be deduced from the data, as that leading to a reduction of the signal to about half of its value. If we accept the SAXS results as the maximum signal, we find for the frequency characteristic for the surface melting in PEO a value around 0.008 s^{-1}, i.e. a characteristic relaxation time on the order of 120 s. This time is 20 times higher than that found for PE.

The reorganization of the crystallite surfaces is obviously a complex procedure, different from a simple Debye process with a unique relaxation time. Figure 26 shows the frequency dependence of the maximum value of the dynamic specific heat for PEO as obtained from all HWS and TMDSC measurements together. Considering that one has reached neither the low frequency end nor the high-frequency end, it is clear that the relaxation curve extends over a frequency range of at least four decades. Hence, surface melting and crystallization uses a whole group of relaxation processes.

Conclusion

Our measurements of the dynamic heat capacity combined with a temperature dependent SAXS structure analysis demonstrate for PE and PEO the existence of surface crystallization and melting as a reversible process. Its dynamics could be resolved by employing both temperature-modulated differential scanning calorimetry (TMDSC) and heat wave spectroscopy (HWS), thereby covering a total frequency range from 10^{-3} to 10^2 Hz. The characteristic times of surface crystallization and melting as measured for temperatures near to the final crystallite melting are about 12 and 120 s for PE and PEO, respectively. Determinations of the dynamic heat capacity $c^*(\omega)$ of samples by TMDSC and HWS require in general the application of appropriate correction procedures on the measured raw data in order to account for the inner heat flow resistance and additional heat capacities of the measuring devices. This can be achieved for both setups by a proper modeling of the main components and functions.

Acknowledgment. Support of this work by the Deutsche Forschungsgemeinschaft (Sonderforschungsbereich 428 and Graduiertenkolleg "Strukturbildung in Makromolekularen Systemen") is gratefully acknowledged. Thanks are also due to the "Fonds der Chemischen Industrie" for financial help.

References and Notes

(1) Ishikiriyama, K.; Wunderlich, B. *Macromolecules* **1997**, *30*, 4126.
(2) Wurm, A.; Merzlyakov, M.; Schick, C. J. *Macromol. Sci.—Phys.* **1999**, *38*, 693.
(3) Androsch, R. *Polymer* **1999**, *40*, 2805.
(4) Saruyama, Y. *Thermochim. Acta* **1999**, *330*, 101.
(5) Schawe, M.; Strobl, G. *Polymer* **1997**, *39*, 3745.
(6) Toda, A.; Tomita, C.; Hikosaka, M.; Saruyama, Y. *Polymer* **1997**, *38*, 2849.
(7) Hu, W.; Albrecht, T.; Strobl, G. *Macromolecules* **1999**, *32*, 7548.
(8) Strobl, G. *The Physics of Polymers*; Springer: Berlin, 1997; p 185ff.
(9) Eischer, E. W. *Kolloid Z. Z. Polym.* **1967**, *218*, 97.
(10) Rieger, J.; Mansfield, M. L. *Macromolecules* **1989**, *22*, 3810.

(11) Tanabe, Y.; Strobl, G.; Fischer, E. W. *Polymer* **1986**, *27*, 1147.
(12) Albrecht, T.; Strobl, G. R. *Macromolecules* **1995**, *28*, 5827.
(13) Goderis, B.; Reynaers, H.; Mathot, V. B. F. *Macromolecules* **2001**, *34*, 1779.
(14) Merzlyakov, M.; Schick, C. *Thermochim. Acta* **1999**, *330*, 65.
(15) Albrecht, T.; Armbruster, S.; Stuehn, B.; Vogel, K.; Strobl, G. *Thermochim. Acta*, in press, 2001.
(16) Strobl, G. *Acta Crystallogr.* **1970**, *A26*, 367.
(17) Strobl, G. *The Physics of Polymers*; Springer: Berlin, 1997; p 408.
(18) Ruland, W. *Colloid Polym. Sci.* **1977**, *255*, 417.
(19) ATHAS data bank. http://web.utk.edu/athas/databank.

MA0106595